RSC Advances

ROYAL SOCIETY OF CHEMISTRY

PAPER

View Article Online
View Journal | View Issue

Check for updates

Cite this: *RSC Adv.*, 2026, **16**, 25675

Dual-mode N_4O_3 tripodal hemi-salen Schiff base sensor for selective colorimetric detection of Ni^{2+} and fluorometric sensing of Zn^{2+}: analytical applications across food, environmental, and forensic matrices

Dishen Kumar,[a] Srishti Dutta,[a] Rajat Kumar Roy,[a] Devanand Sahu,[a] Abhilash Pandey,[a] Vanshika Sharma,[a] Anjali Suryavanshi[b] and Goutam Kumar Patra *[a]

Received 24th February 2026
Accepted 8th May 2026

DOI: 10.1039/d6ra01601d

rsc.li/rsc-advances

Tris-(2-aminoethyl) amine and 3,5-Di-*tert*-butyl-2-hydroxybenzaldehyde are the sources of the tripodal N_4O_3 donor tris-Schiff base hemi-salen molecular probe **L**, which we have presented here for the sensitive and selective colorimetric detection of Ni^{2+} and turn-on fluorometric detection of Zn^{2+} in aqueous media over a range of other competing cations. The detection limits are 9.4×10^{-7} M and 4.68×10^{-7} M, respectively. The FT-IR, ESI-mass, and Job-plot spectrum analyses confirmed a 1 : 1 stoichiometry between the **L** and Zn^{2+} and **L** and Ni^{2+} ions. Using Na_2EDTA, the reversible reactivity to the Ni^{2+} and Zn^{2+} ions has been demonstrated. Moreover, **L** can function across a broad pH range and is helpful for detecting and quantifying Ni^{2+} and Zn^{2+} in food and environmental materials. In a variety of forensic applications, it aids in the creation of latent fingerprints. Molecular docking studies of **L** have also been reported here as preliminary computational insight into possible biomolecular interactions.

1 Introduction

Studies on metal ion sensing is still crucial for biological systems and the environment.[1,2] Nickel is one of the important components in the transition metal series, required for biological processes like respiration, metabolism, and biosynthesis.[3,4] It is an essential part of several metalloenzymes, such as hydrogenases, acireductone dioxygenases, and carbon monoxide dehydrogenases.[5–7] Its existence in the environment is specifically caused by a variety of natural processes, including weathering, erosion, and volcanic eruptions. Furthermore, nickel is found naturally in foods including chocolate, cocoa, coffee, tea, plants like broccoli, spinach, asparagus, carrots, and tomatoes, and legumes like green beans and almonds.[8–10] It is extensively utilised in the chemical industry for electroplating, electroforming, and the production of useful electronics such as Ni-Cd batteries.[11–15]

It has long been believed that nickel is a potentially hazardous metal. At 2.5 mg mL^{-1}, Ni^{2+} ion levels in drinking water are acceptable. Ni^{2+} can readily penetrate the aquatic milieu and have detrimental effects on the environment because of its extensive metallurgical use in industrial processes.[16–19] Diseases of the central nervous system, lung cancer, allergies, pneumonia, and respiratory issues are among the physical health effects of excessive Ni^{2+} accumulation above recommended threshold limit.[20–22] Thus, one of the difficult issues in the current research is the precise ability to detect the Ni^{2+} ion at the biological and environmental level.

Similarly, Zn^{2+}, which is present in metalloproteins, is the second most common trace element in the human body.[23] Zn^{2+} is essential for cellular metabolism, neural signaling, cell apoptosis, and other processes in the human body. Zn^{2+}-containing compounds may be employed as anticancer medications, insulin mimetics, antimicrobials, antidiabetic, radioprotectives, and tumor photosensitizers.[24–26] Meanwhile, a common industrial waste, Zn^{2+}, accumulates in ecosystems and seriously contaminates the water. Zn^{2+} imbalance in organisms has a major impact on a number of human illnesses, such as mental disorders, Parkinson's disease, infantile diarrhea, Alzheimer's disease, ischemic stroke, epilepsy, delayed sexual maturation, Wilson's diseases, and amyotrophic lateral sclerosis (ALS).[27–30] Zinc is a common contaminant in food and agricultural wastes, and too many Zn^{2+} ions can have phytotoxic effects and reduce soil microbial activity.[31,32] Therefore, a highly sensitive and reliable Zn^{2+} sensor is needed to monitor its presence and content in organisms and environments.

Given the relevance of heavy transition metal ions in biological, environmental, and industrial processes, there has been a significant focus on the design and synthesis of effective chemo-receptors for their detection and measurement. In the

---

[a] *Department of Chemistry, Guru Ghasidas Vishwavidyalaya, Bilaspur, C. G, India. E-mail: patra29in@yahoo.co.in; Tel: +917587312992*

[b] *Department of Pharmacy, Guru Ghasidas Vishwavidyalaya, Bilaspur, C. G, India*

last few years, a variety of conventional analytical methods have been used to detect heavy metal ions, including atomic absorption spectroscopy (AAS),[33] flow-injection amperometry,[34] chromatography,[35] potentiometry,[36] and inductively coupled plasma emission spectroscopy (ICP-ES).[37] Most of these methods, however, have serious drawbacks, including poor sensitivity, selectivity, time commitment, challenging sample preparation, a need for highly qualified staff, and the use of expensive and complex equipment.

In recent years, optical signaling-based chemosensors have become a viable tool among the other realistic techniques due to their operational advantages, on-site and actual analysis, good selectivity, and sensitivity.[38–40] Additionally, it would be more efficient and less expensive to use a single receptor to detect several targets, including various analyte types, as opposed to a one-to-one analysis technique. It would therefore attract greater attention.[41–43]

In this study, we have described a tripodal N_4O_3 donor tris-Schiff base molecular probe **L**, which is formed by condensation of tris(2-aminoethyl)amine (tren) and 3,5-di-*tert*-butyl-2-hydroxybenzaldehyde, for colorimetric detection of Ni^{2+} ions and selective, turn-on fluorometric detection of Zn^{2+} ions. The aforementioned research works and our search for a fluorescent colorimetric chemosensors[44–47] serve as the driving forces behind this endeavour. The receptor showed a clear color change from light yellow to orange yellow for Ni^{2+} ions in a methanol–tris–HCl buffer solution (10 mM, pH 7.2, 1 : 1 v/v) with a detection limit of 9.4×10^{-7} M, and a fluorometric "turn-on" response for Zn^{2+} ions with a detection limit of 4.68×10^{-7} M.

Although Schiff base-based chemosensors for transition metal ions are well established, the present work offers several distinct advances. First, the designed probe features a rare tripodal N_4O_3 hemi-salen architecture, providing a preorganized multidentate binding cavity that differs fundamentally from conventional planar Schiff base systems.[48] Second, it exhibits true orthogonal dual-mode sensing, enabling selective colorimetric detection of Ni^{2+} *via* LMCT and fluorescence turn-on detection of Zn^{2+} *via* a CHEF mechanism within a single molecular platform. Such differentiation of two metal ions through independent signaling pathways remains scarcely reported.[49] Third, the probe demonstrates multifunctional applicability, extending beyond solution-phase sensing to real sample analysis and latent fingerprint visualization.[50] These combined structural, mechanistic, and application-level features collectively establish the present system as a meaningful advancement over recent Schiff base-based chemosensors for metal ions.

2 Experimental

2.1 Materials and equipment

Sigma Aldrich is the supplier of metal salts, 3,5-Di-*tert*-butyl-2-hydroxybenzaldehyde, and tris-(2 aminoethyl)amine. For all studies, analytical-grade solvents were utilized, and a solution of tris buffer (pH = 7.2) was prepared using double-distilled water for dilution. Their nitrate salts were used to make the metal ion solutions. A Shimadzu UV 1800 spectrophotometer was used to capture absorption spectra using quartz cuvettes with a wavelength between 200 and 800 nm and a path length of 10 mm. A Shimadzu RF 5000 Fluorescence Spectrometer was used to record the luminescence spectra. A Waters mass spectrometer was used to record high-resolution mass (HRMS) spectra using a mixed solvent HPLC consisting of triple-distilled water and methanol. The Bruker Alpha II FTIR spectrophotometer was used to record the FTIR spectra (KBr disk). A Bruker DRX spectrometer running at 400 MHz was used to record the ^1H and ^{13}C NMR spectra. The chemical shift was measured in ppm in relation to TMS. A digital pH meter (Merck) was used to measure the pH by changing sodium hydroxide and diluted hydrochloric acid in a buffer solution. Methanol–tris–HCl buffer solution (10 mM, pH 7.2, 1 : 1 v/v) and H_2O were used to prepare solutions of the receptor **L** (1×10^{-5} M) and metal salts (1×10^{-4} M), respectively.

2.2 Synthesis of tripodal N_4O_3 donor tris-Schiff base hemi-salen ligand (L)

A mixture of 3,5-Di-*tert*-butyl-2-hydroxybenzaldehyde (702 mg, 3 mmol) and tris-(2-aminoethyl) amine (146 mg, 1 mmol) is heated under reflux in distilled methanol for six hours. After removing any suspended items using a filter, the resultant yellow solution is allowed to slowly evaporate, allowing the **L** to precipitate as a yellow solid. Yield, 0.684 gm, 86%. Melting point 88 °C. Anal. Calc. for $C_{51}H_{78}N_4O_3$: C, 77.03; H, 9.89; N, 7.05. Found C, 77.01; H, 9.82; N, 7.05%. ^1H NMR (400 MHz, $CDCl_3$, TMS): δ (ppm) 13.91 (s, 3H, OH), 8.34 (s, 3H, HC = N), 7.38 (s, 3H, Ar–CH), 7.04 (s, 3H, Ar–CH), 3.68 (t, 6H, J = 6.0 Hz, $C{=}NCH_2$), 2.97 (t, 6H, J = 6.3 Hz, N–CH_2), 1.45 (s, 27H, C–$(CH_3)_3$), and 1.31 (d, 27H, C–$(CH_3)_3$) (Fig. S1). ^{13}C NMR (100 MHz, $CDCl_3$, TMS): δ (ppm), 166.77 (HC = N), 158.14, 139.93, 136.62, 126.83, 125.81 and 117.88 (Ar–CH), 58.31 and 55.97 (CH_2), 35.02 and 34.12, (C–$(CH_3)_3$, 31.53 and 29.72 (C–$(CH_3)_3$ (Fig. S2). FTIR/cm^{-1} (KBr): 3856 (wb), 3743 (m, –OH), 3213 (m, –NH), 2990 (s, aliphatic –CH), 1623 (*vs.*, C=N), 1546 (s, –C=C)), 1448 (*vs.*, –C=C), 1360 (m), 1250 (m, –C–N), 1170 (s), 1030 (m), 875 (m), 776 (s), 690 (m). (Fig. S3). ESI MS: 796.7438 $[M–H]^+$ (Fig. S4).

2.3 UV-vis titration

By dissolving **L** (7.95 mg, 0.01 mmol) in the solvent mixture CH_3OH–H_2O (1 : 1, v/v) (10 mL) and diluting 30 μL of it with the solvent mixture to 3 mL, a final concentration of 10 μM was obtained. The guest cations solution was prepared separately using triple-distilled water and their nitrate salts in the range of 10 mM. It was then further diluted to the proper concentration. After a short time elapsed combining **L** with each of the metal ions, UV-vis spectra were recorded at room temperature.

2.4 Fluorescence titration

After dissolving $Zn(NO_3)_2 \cdot 6H_2O$ (29.7 mg) in 10 mL of triple-distilled water, 15–90 μL of this Zn^{2+} solution (10 mM) was added to each receptor solution (10 μM) to yield 0.5–30 equiv. **L** (7.95 mg, 0.01 mmol) was dissolved in the same solvent (10 mL) to prepare a solution, and 30 μL of this solution were diluted with 3 mL of solvent mixture to achieve a final concentration of 10 μM. The fluorescence spectra were obtained at room temperature after a short mixing time.

2.5 Job plot measurements

100, 90, 80, 70, 60, 50, 40, 30, 20, 10, and 0 μL of the **L** solution were obtained and put in vials after **L** (7.95 mg, 0.01 mmol) was dissolved in 10 mL of methanol. $Ni(NO_3)_2\cdot 6H_2O/Zn(NO_3)_2\cdot 6H_2O$ (0.01 mmol) were dissolved in 10 mL of triple-distilled water after each vial was diluted with 2.9 mL of a mixed solvent. Each diluted **L** solution received 0, 10, 20, 30, 40, 50, 60, 70, 80, 90, and 100 μL of the Ni^{2+}/Zn^{2+} solution, making a total volume of 3 mL. After shaking the vials for a minute, they were left to settle before room temperature UV-Vis spectra were taken.

2.6 pH effect test

100 mM HEPES buffer was used to prepare a range of buffers with pH values between 2 and 12. The receptor **L** (7.95 mg, 0.01 mmol) was dissolved in 10 mL of methanol after the pH of the solution was achieved. Using the aforementioned buffers, 30 μL of this solution (1 mM) was further diluted to 3 mL to achieve a final concentration of 10 μM. Ten milliliters of HEPES buffer (pH 7.00) were used to dissolve 0.1 mmol of $Ni(NO_3)_2\cdot 6H_2O/Zn(NO_3)_2\cdot 6H_2O$. For every previously generated 10 μM receptor solution, 30 μL of the Ni^{2+}/Zn^{2+} solution (10 mM) was added. Fluorescence spectra were acquired at room temperature after a short mixing time.

2.7 Competition with other metal ions

After dissolving **L** (7.95 mg, 0.01 mmol) in the previously mentioned solvent combination (10 mL), 30 μL of it was diluted to 3 mL using the solvent mixture to get a final concentration of 10 μM. $M(NO_3) \times$ (0.1 mmol) and $Ni(NO_3)_2\cdot 6H_2O/Zn(NO_3)_2\cdot 6H_2O$ (0.01 mmol) were dissolved in ten milliliters of triple-distilled water. To obtain 10 equivalents of metal ions, 30 μL of each metal solution (10 mM) was combined with 3 mL of receptor **L** (10 μM) solution. The combined solution of each metal ion and **L** was mixed with 30 μL of Ni^{2+}/Zn^{2+} solution (10 mM) to make 10 equivalents. UV-Vis/fluorescence spectra were acquired at room temperature following a brief mixing period.

2.8 Molecular docking

The protein data bank provided the crystal structures of many protein targets (PDB IDs: 4OUH, 1PXX, 3SFH, and 3RCD), which were then created by eliminating heteroatoms and water molecules. ChemDraw Professional 12.0 was used to draw the hemi salen ligand, **L** and ArgusLab 4.0.1 (MMFF94 force field) was used to decrease its energy. A grid box enclosing the active site was used for docking in ArgusLab 4.1.0, and binding energy was used to determine the optimal position.[51,52] Discovery Studio Visualizer was used to investigate and visualize ligand–protein interactions in both 2D and 3D.

2.9 Computational details

The GAUSSIAN-09 Revision C.01 program package was used for all calculations.[53] The gas phase geometries of the chemosensor **L** was fully optimized without any symmetry restrictions in the singlet ground state with the gradient-corrected DFT level coupled with the hybrid exchange–correlation functional that uses the Coulomb-attenuating method B3LYP.[54] Basis set 6-31++G was found to be suitable for the whole molecule. LanL2DZ basis sets were implemented for the geometry optimization of **L** + Ni^{2+} and **L** + Zn^{2+} complexes.

3 Results and discussion

3.1 Synthesis and structure of the probe L

The organic ligand 6,6′,6″-((1*E*,1′*E*,1″*E*)-((nitrilotris(ethane-2,1-diyl))tris(azaneylylidene)) tris(methaneylylidene))tris(2,4-di-*tert*-butylphenol) (**L**) (Scheme 1) has been obtained in a good yield (86%) by the 1 : 3 condensation reaction of tris-(2 amino-ethyl)amine and 3,5-Di-*tert*-butyl-2 hydroxy-benzaldehyde in dehydrated methanol. It was characterized by ^1H NMR and ^{13}C NMR spectroscopy, FTIR, EI-MS spectroscopy, and elemental analysis. The –OH protons resonate at 13.91 ppm, the phenyl protons between 7.04 and 7.38 ppm, and the –CH=N protons at 8.34 ppm in the probe **L**'s 1H-NMR spectra. The infrared spectra of the tris Schiff base **L** showed that the O–H stretching frequency was 3743 cm^{-1}, the –NH was 3213 cm^{-1}, the aliphatic –CHs were 2990 cm^{-1}, and the C=N was 1623 cm^{-1}. Unfortunately, despite our best efforts in a range of solvents, we were unable to prepare single crystals suitable for X-ray diffraction investigations for **L**.

3.2 UV-vis spectral study of the chemosensor L

In a methanol–tris–HCl buffer medium (10 mM, pH 7.2) solution (1 : 1 v/v), the colorimetric sensing behavior of receptor **L** was examined in the presence of three equivalents of distinct metal ions, including Al^{3+}, Cr^{3+}, Co^{2+}, Fe^{3+}, Cu^{2+}, Zr^{4+}, Cd^{2+}, Fe^{2+}, Hg^{2+}, Ag^{+}, Mn^{2+}, Pb^{2+}, Ni^{2+}, Sr^{2+}, and Zn^{2+}. This was carried out in order to determine receptor **L**'s unique selectivity. Fig. 1 shows that Ni^{2+} was the only metal ion to exhibit a discernible colour change from yellow to orange; other metal ions did not. The similar colour change under UV light was depicted in Fig. S5. The receptor **L** displays primary absorption bands at 270 and 346 nm as a result of S0–S1 transitions. Only when three equivalents of Ni^{2+} ions are present does the absorption band at 346 nm undergo a blue shift up to 22 nm, and a new absorption band at 415 nm is formed (Fig. S6). There was no peak at 415 nm when the same amount of different metal ions were added. The higher coordination capacity of the Ni^{2+} ion with **L** over the other ions may be the cause of the colour change and spectrum shift that occurs upon the addition of Ni^{2+} ions. The ability of chemosensor **L** to detect metal ions was further investigated using absorption titration tests.

The addition of Ni^{2+} results in a distinct bathochromic shift and the appearance of a new low-energy absorption band in the visible region. Such spectral features are characteristic of ligand-to-metal charge transfer (LMCT) transitions, where

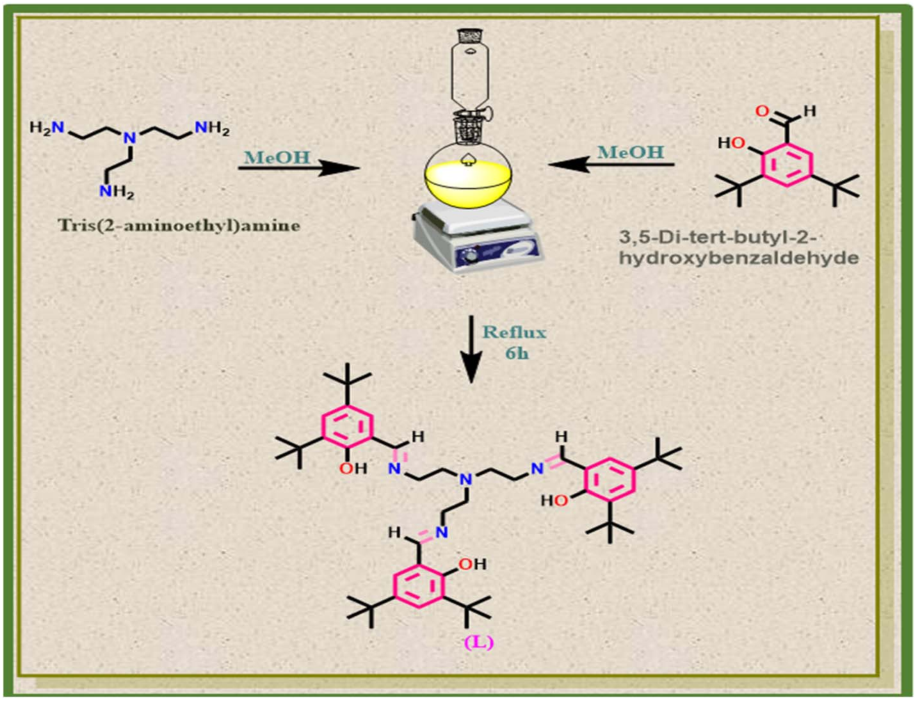

Scheme 1 Synthetic procedure of the receptor L.

Fig. 1 Colour changes of L after the addition of 3 equiv. of different cations in methanol–water (1 : 1, v/v).

electron density is transferred from ligand donor atoms (O/N) to the partially filled Ni^{2+} d-orbitals. The intensity and position of this band increase systematically with Ni^{2+} concentration, confirming complex formation and charge-transfer interaction rather than simple aggregation or solvatochromic effects.

To further understand the sensitivity response of chemosensor **L** towards Ni^{2+} ions, the UV-vis titration experiment was conducted by recording the different concentrations of Ni^{2+} ions individually. When seven equivalents of Ni^{2+} were added to **L**, the absorption bands at 346 nm gradually expanded and blue-shifted (up to 21 nm), and a new absorbance band emerged at 396 nm (Fig. 2). The isosbestic point at 325 nm (Fig. 2) indicates that only one complex species was generated between **L** and Ni^{2+}. The formation of a complex between the Ni^{2+} and receptor **L**, known as ligand-to-metal charge transfer (LMCT), is made more likely by a blue shift in the chromophore **L**'s Ni^{2+} absorption spectra. The ligand-to-metal charge-transfer (LMCT) mechanism may be represented by the orange colour.

The calibration curves of titration tests demonstrated that the absorbance intensity of the metal ion Ni^{2+} at 396 nm changed roughly linearly with concentration. Thus, the detection limit for Ni^{2+} was found to be 9.4×10^{-7} M using the standard formula $DL = 3\sigma/m$, where "σ" is the standard deviation of the blank measurement and "m" is the slope of the linear calibration curve (Fig. 3). The WHO drinking water recommendation and other documented Ni^{2+} sensors are far higher than these low level DL readings. According to the WHO, the maximum concentration of Ni^{2+} ions that can be found in drinking water is 0.0008 mg L^{-1}.[55]

By linearly fitting graph $1/(A - A_0)$ $1/[Ni^{2+}]^{1/2}$, the association constants were computed using the Benesi–Hildebrand (B–H) equation under the assumption of a 1 : 1 host–guest ratio' The measured values of 1.86×10^3 $M^{-1/2}$ show that receptor **L** and the analyte Ni^{2+} have a very high affinity (Fig. S7).

A chemosensor **L**'s tolerance limit to other interfering ions and excellent metal ion selectivity are two crucial characteristics. UV-Vis spectra of the receptor **L** in the presence of many

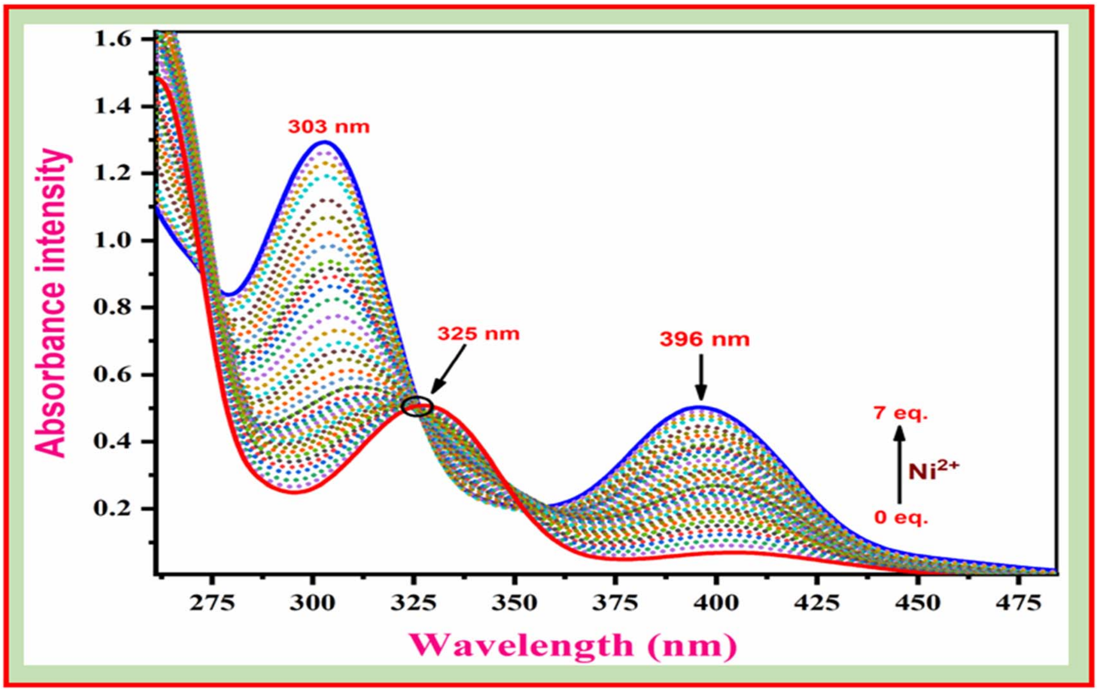

Fig. 2 UV-vis titration curves of L with Ni^{2+} in CH_3OH-H_2O (1 : 1, v/v), at different concentrations of Ni^{2+}.

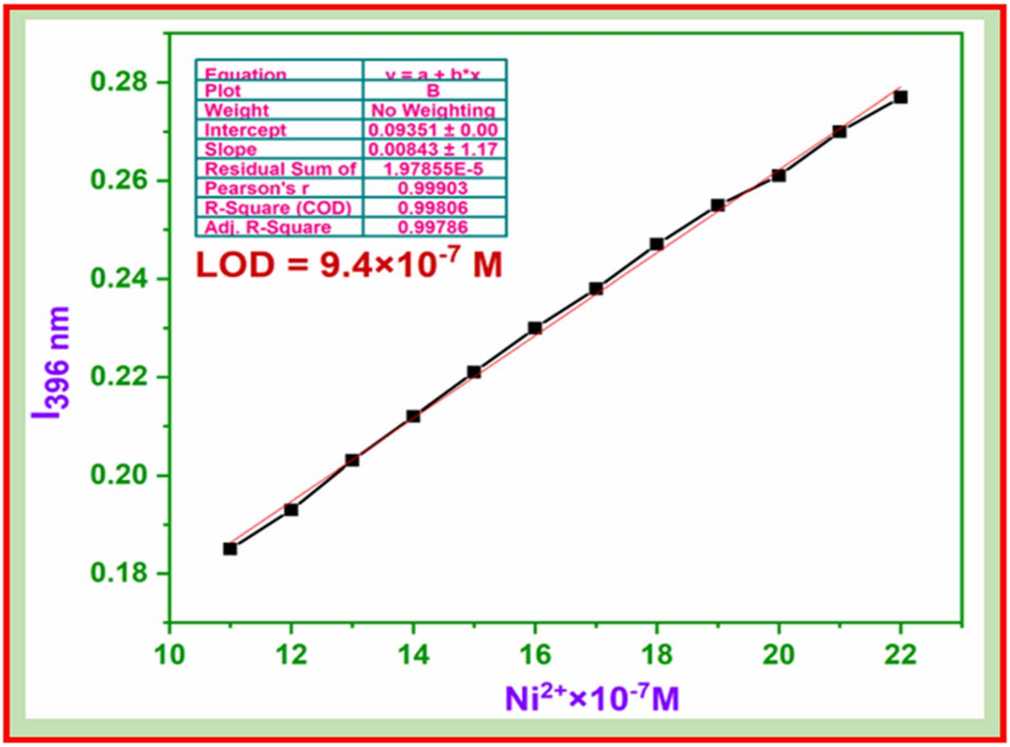

Fig. 3 Standard deviation and linear fittings for detection limit calculations of L for Ni^{2+} based on UV-Vis titration method.

ions (Al^{3+}, Cr^{3+}, Co^{2+}, Fe^{3+}, Cu^{2+}, Zr^{4+}, Cd^{2+}, Fe^{2+}, Hg^{2+}, Ag^{+}, Mn^{2+}, Pb^{2+}, Ni^{2+}, Sr^{2+} and Zn^{2+}) were acquired in order to assess the selectivity of the receptor for the detection of Ni^{2+} ions (Fig. 4). The simultaneous presence of other metal ions in the solution had no effect whatsoever on the intensity of the absorption band produced at 396 nm as a result of the formation of the **L**-Ni^{2+} complex. Dilution effects only cause a modest drop in colour intensity. The process of improving absorbance

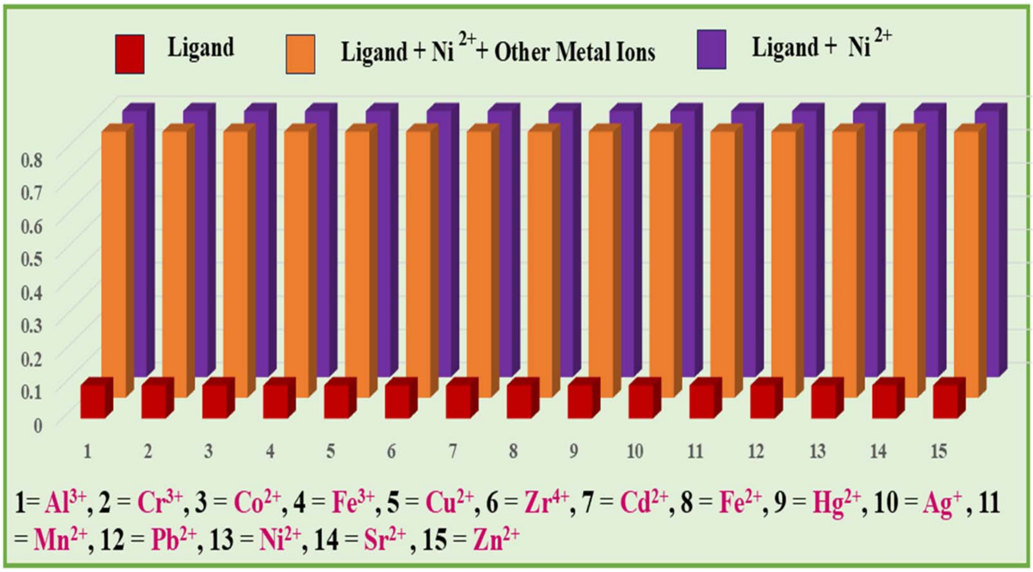

Fig. 4 Absorbance interference test of L with different metal ions.

is unaffected by the other metals. Therefore, even at three times the background ion concentration, the proposed chemosensor **L** exhibits selectivity towards Ni^{2+} ions.

Disodium ethylene diamine tetra acetic acid (Na$_2$EDTA), a common metal chelator, has been used to study the reversibility of chemosensor **L**. When three equivalents of Ni^{2+} ions are added to the probe (**L**) solution, the mixture's colour changes from light yellow to orange yellow. If the **L** + Ni^{2+} adduct was treated with three equivalents of the strong chelator Na$_2$EDTA, the absorbance bands at around 396 nm with the orange-coloured solution of the host–guest complex instantly turned yellow (Fig. 5). Repeated introduction of Ni^{2+} ions nearly restored the colour and spectrum changes. Even after three cycles in which the chelator and analyte were introduced alternately, the switching behaviour between **L** and **L** + Ni^{2+} complexes remained unchanged.

The pH of the media has a major impact on receptor **L**'s capacity to detect Ni^{2+} ions. The **L**-Ni^{2+} complex and free **L** absorption intensities were determined at various pH values, which were corrected using diluted HCl and NaOH. The strength of free receptor **L** gradually increases until pH ~7, after which it decreases, indicating partial deprotonation effects and receptor instability in extremely basic or acidic conditions. In contrast, over the whole pH range that was evaluated, the **L**-Ni^{2+} combination shows a notably higher intensity. Around pH 7, it peaks, and as the pH approaches alkaline, it begins to decline. This suggests that strong acidic or basic conditions decrease binding efficiency, even if complex formation is most stable and

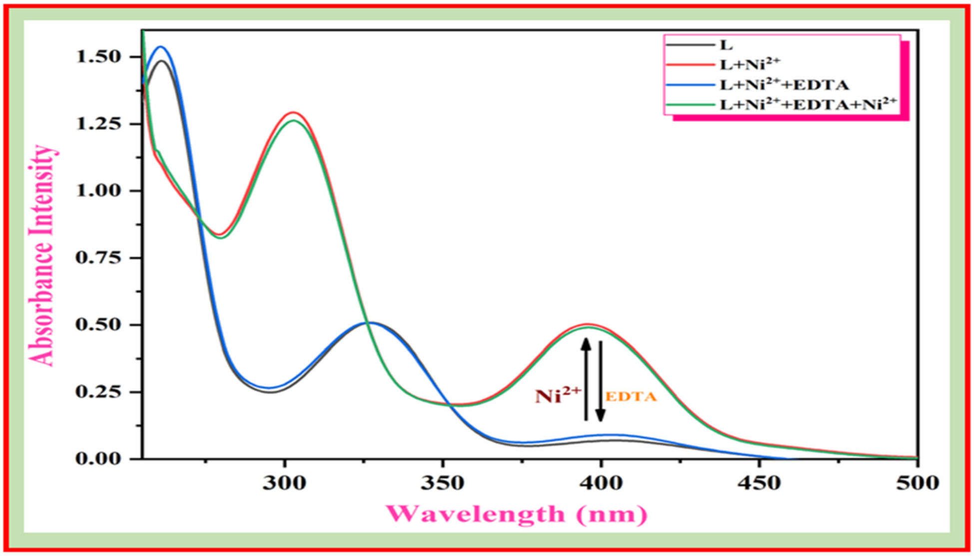

Fig. 5 UV-Visible absorbance spectra of L in the absence and presence of Ni^{2+} and Na$_2$EDTA.

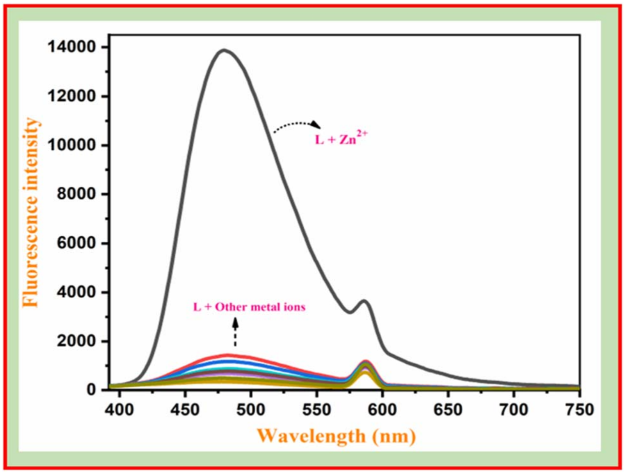

Fig. 6 Emission spectra of **L** (10 mM in $CH_3OH–H_2O$; 1 : 1, v/v) in presence of different metal ions (Al^{3+}, Cr^{3+}, Co^{2+}, Fe^{3+}, Cu^{2+}, Zr^{4+}, Cd^{2+}, Fe^{2+}, Hg^{2+}, Ag^{+}, Mn^{2+}, Pb^{2+}, Ni^{2+}, Sr^{2+} and Zn^{2+}).

effective at neutral pH. Overall, the findings show that receptor **L** is sensitive to pH and that it is best able to detect Ni^{2+} ions in the pH 5–8 range, which is consistent with physiological systems (Fig. S8).

3.3 Fluorescence studies

The emission properties of receptor **L** in the presence of specific metal ions were further examined in a mixture of methanol and tris HCl buffer (10 mM, pH 7.2, 1 : 1 v/v). Under a UV lamp, **L** shows light bluish-yellow colorization and minimal emission at 485 nm with a poor fluorescence quantum yield ($\Phi = 0.0068$) upon stimulation at 360 nm at room temperature. Of the selected metal ions, Al^{3+}, Cr^{3+}, Co^{2+}, Fe^{3+}, Cu^{2+}, Zr^{4+}, Cd^{2+}, Fe^{2+}, Hg^{2+}, Ag^{+}, Mn^{2+}, Pb^{2+}, Ni^{2+}, Sr^{2+} and Zn^{2+}, only the addition of three equivalents of Zn^{2+} ions to the ligand **L** solution significantly increased the emission intensity at 480 nm. The emission of the receptor **L** was not significantly increased by the same quantity of other metal ions, including Ni^{2+} (Fig. 6).

The free ligand **L**, exhibits weak emission, whereas upon Zn^{2+} addition, a significant fluorescence enhancement ("turn-on") is observed. Importantly, this enhancement occurs without major shift in emission wavelength, indicating that the electronic transition remains ligand-centered and is not due to a new emissive species. This behaviour is consistent with chelation-enhanced fluorescence (CHEF), where coordination suppresses non-radiative decay pathways increases the quantum yield.

To get the detailed characteristics of the emission spectra, Zn^{2+} ions were added progressively in a titration experiment. As the concentration of Zn^{2+} ions in the receptor solution rose, the emission intensity gradually increased up to 53 times with a slight blue shift, achieving saturation at 6 equiv. of Zn^{2+} ions (Fig. 7). The metal ion connection with receptor **L** *via* the imine side most likely impeded the non-radiative PET and >C=N isomerization processes, which resulted in an increase in emission intensity due to the chelation enhanced fluorescence effect (CHEF). But for the Ni^{2+} ion, the emission intensity of **L** remains unchanged, suggesting that the opposing mechanisms of paramagnetic fluorescence quenching and chelation increasing

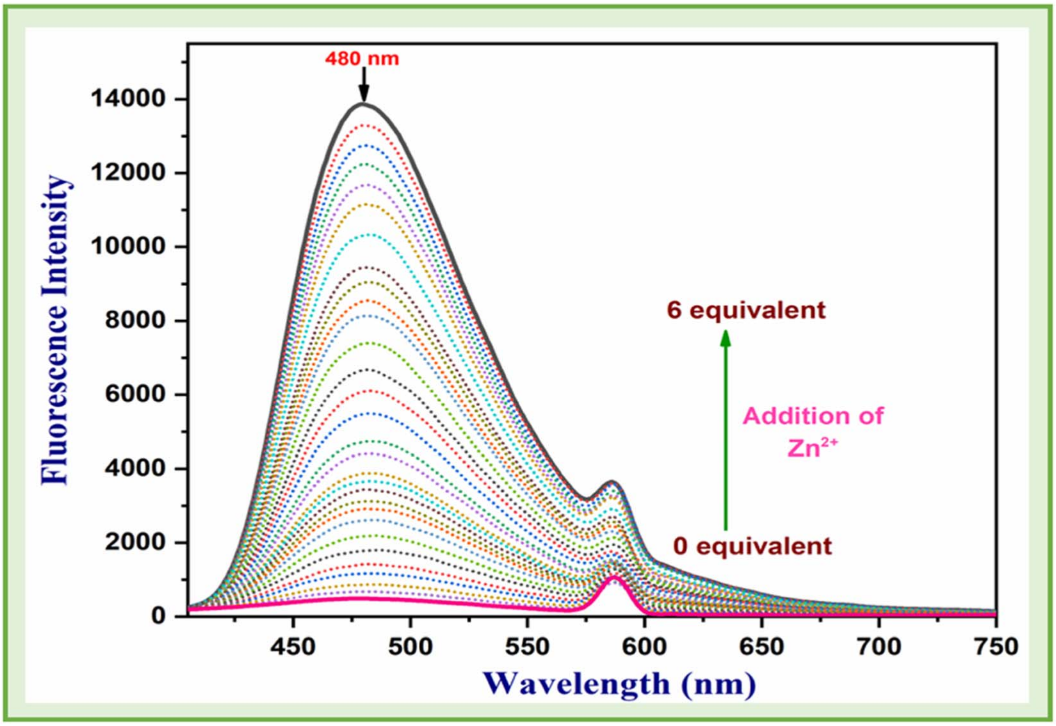

Fig. 7 Emission titration of **L** in the presence of different amounts of Zn^{2+} ion in ($CH_3OH–H_2O$; 1 : 1, v/v).

fluorescence impact mutually compensate in the **L**-Ni^{2+} complex.[56,57] To examine the selectivity of the receptor **L** for the detection of Zn^{2+} ions, we analyzed the fluorescence spectra of the ligand **L**, **L** + Zn^{2+} ions, and **L** + Zn^{2+} ion + other metal ions. Using fluorescence data and the Benesi–Hildebrand (B–H) equation, the association constants were determined to be 1.2×10^5 $M^{-1/2}$ (Fig. S9), assuming a 1 : 1 host–guest ratio. This indicates a very high affinity between receptor **L** and the analyte Zn^{2+}.

We observed that the fluorescence intensity of the **L**-Zn^{2+} adduct at 480 nm is unaffected by the presence of other metal

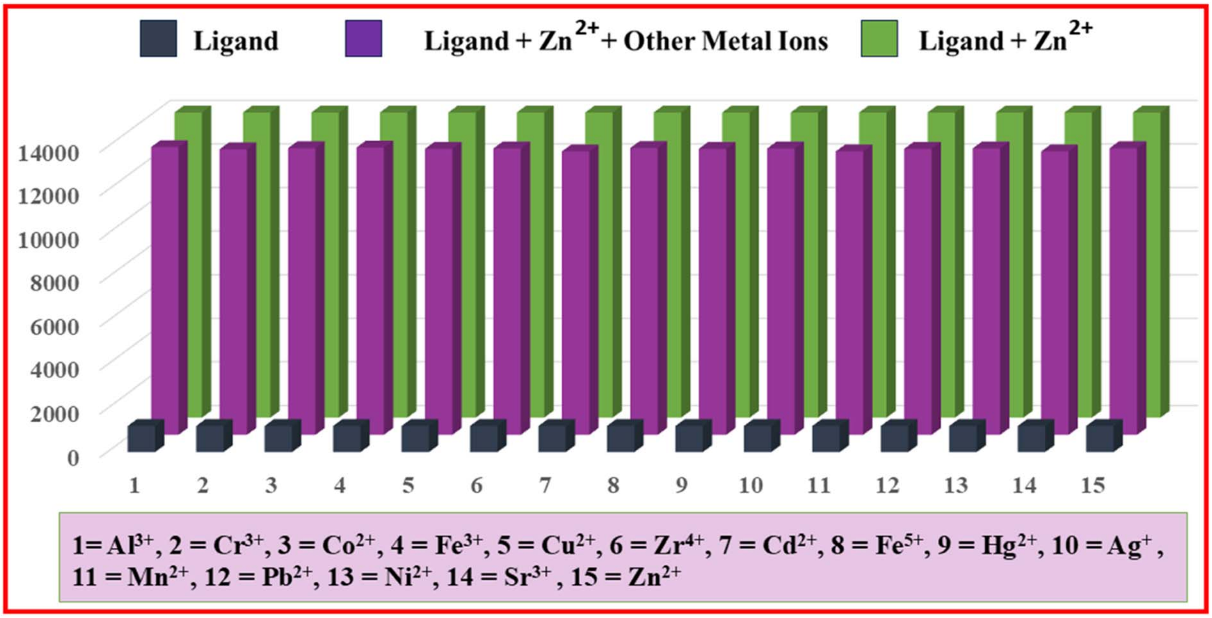

Fig. 8 Emission spectra of L at 480 nm in presence of Zn^{2+} and different metal ions.

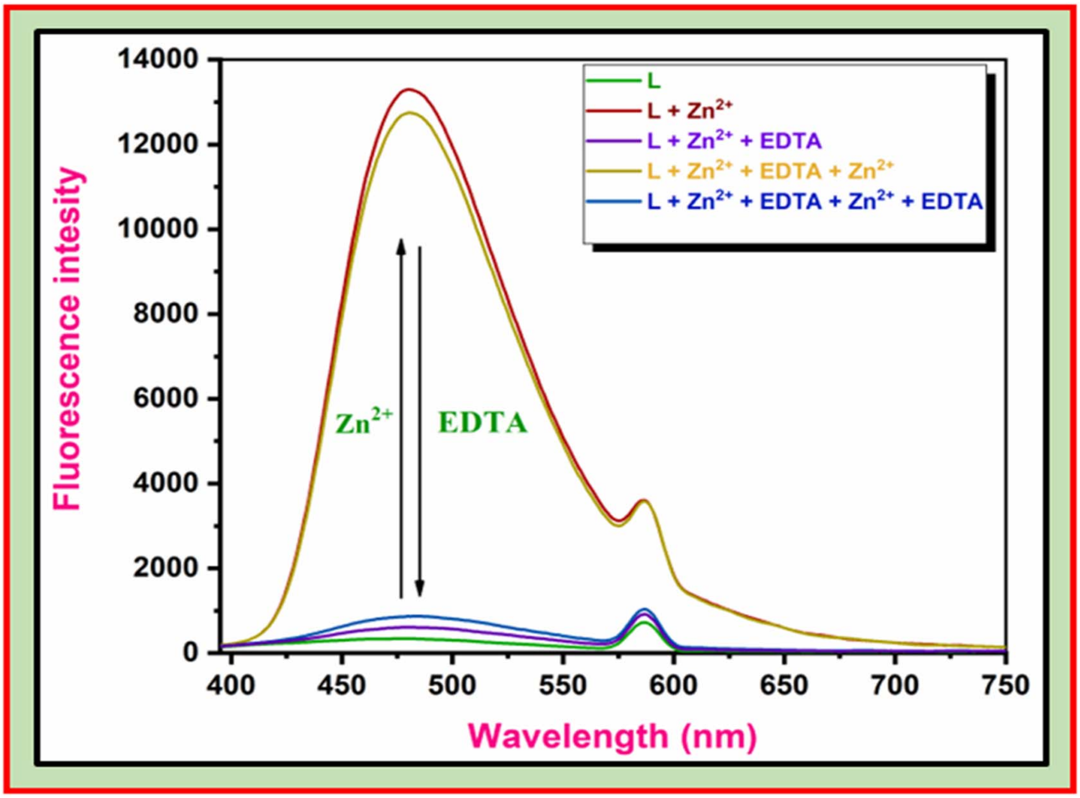

Fig. 9 Emission spectra of L in the absence and presence of Zn^{2+} and Na_2EDTA.

ions (Fig. 8). The fluorometric detection limit was found to be 4.68×10^{-7} M using the same formula $3\sigma/m$ (Fig. S10). Stable chelate complexes are typically formed by metal ions such as Zn^{2+} with the multidentate ligand Na_2EDTA. Fluorescence measurements using **L** + Zn^{2+} solution and Na_2EDTA as the working medium verified reversibility. The characteristic emission bands of the host–guest combination at 480 nm disappeared as soon as the **L** + Zn^{2+} adduct interacted with three equivalents of Na_2EDTA (Fig. 9). After adding three equivalents of the analyte Zn^{2+}, the emission intensity at 480 nm nearly recovered, indicating that the sensing process is more reversible than any irreversible reaction that the metal ion Zn^{2+} may have enabled.

3.4 Sensing mechanism

To ensure the binding positions of sensor colorimetric and fluorometric responses of **L**, the stoichiometries of **L** + Ni^{2+}/Zn^{2+} were calculated using Job's plot. According to Job's plot between the relative colorimetric intensity fluctuation at 396 nm and the fluorometric intensity variation at 480 nm, the **L**-Ni^{2+} and **L**-Zn^{2+} complexes had 1 : 1 stoichiometries, with mole fractions (χ_M) of 0.51 and 0.50, respectively (Fig. S11).

The **L**-Ni^{2+} and **L**-Zn^{2+} adducts were studied utilizing mass spectral and infrared spectral analysis to better understand the sensing process. According to the ESI-mass spectra, [**L**-Ni^{2+}] and [**L**-Zn^{2+}] were responsible for the molecular ion peaks at m/z = 852.2938 (Fig. S12) in the **L**-Ni^{2+} adduct and m/z = 859.0926 (Fig. S13) in the **L**-Zn^{2+} adduct, respectively. The broad band in the infrared spectra of the free ligand **L**, which is centered at 1623 cm^{-1}, is caused by the imine moiety of the C═N groups. In the Ni^{2+} complex of **L**, the band shifts to 1610 cm^{-1}, indicating a shift towards lower wave numbers and the possible involvement of the azomethine group in the metal ions' interaction with the ligand (Fig. S14). The FT-IR spectra of the **L**-Zn^{2+} adduct were similar to that of **L**-Ni^{2+} .

The analyte's detection of the binding site and signal transduction pathway is the main factor causing metal sensing. One unit of 3,5-di-*tert*-butyl-2-hydroxybenzaldehyde and the imine part of tris-(2-aminoethyl) amine function as a signalling component, while the two –OH groups of two units of 3,5-Di-*tert*-butyl-2-hydroxybenzaldehyde and three imine Ns from tris-(2-aminoethyl) amine in **L** serve as a pocket suitable for metal coordination. First, complexation at the acceptor site is seen in the absorption spectra. In the ground state, this improves the ICT process and leads to colorimetric sensing. The non-radiative PET and >C═N isomerization processes were probably hindered by the Zn^{2+} coordination with receptor **L** *via* the imine side. This led to an increase in emission intensity because of the chelation-enhanced fluorescence effect (CHEF). In the **L**-Ni^{2+} adduct, the quenching of paramagnetic fluorescence mutually compensates. Scheme 2 illustrates the probe **L**'s most probable sensing mechanism.

3.5 DFT studies on the ligand and its Ni^{2+} and Zn^{2+} complexes

Density functional theory (DFT) calculations on the ligand **L** were carried out to determine the most probable structure of **L**. Fig. 10 displays the geometrically optimised structure as well as a schematic depiction of the energy of MOs and the outlines of certain HOMO and LUMO orbitals of **L**. 2.86 eV is the estimated energy difference between HOMO and LUMO in **L**.

In order to get a close approach towards the probable binding mechanism, density functional theory calculations of the respective Ni^{2+} and Zn^{2+} complexes were performed. The geometry optimized structures and a schematic representation of the energy of MOs and contours of selected HOMO and LUMO orbitals of both **L**-Ni^{2+} and **L**-Zn^{2+} complexes have been shown in Fig. S15 and 11, respectively. Notably, the calculated energy gaps between HOMO and LUMO decreased from **L** (2.86 eV) to its M^{2+} complexes (for M = Ni, 0.47 eV; and M = Zn, 1.39 eV). Such lowering of the HOMO–LUMO energy gaps of the ligand **L** upon Ni^{2+} and Zn^{2+} complexation is attributed to the electron redistributions, which resulted in the change in absorbance and fluorescence spectra, respectively. We were unable to grow single crystals of neither the **L**-Ni^{2+} nor the **L**-Zn^{2+} complex.

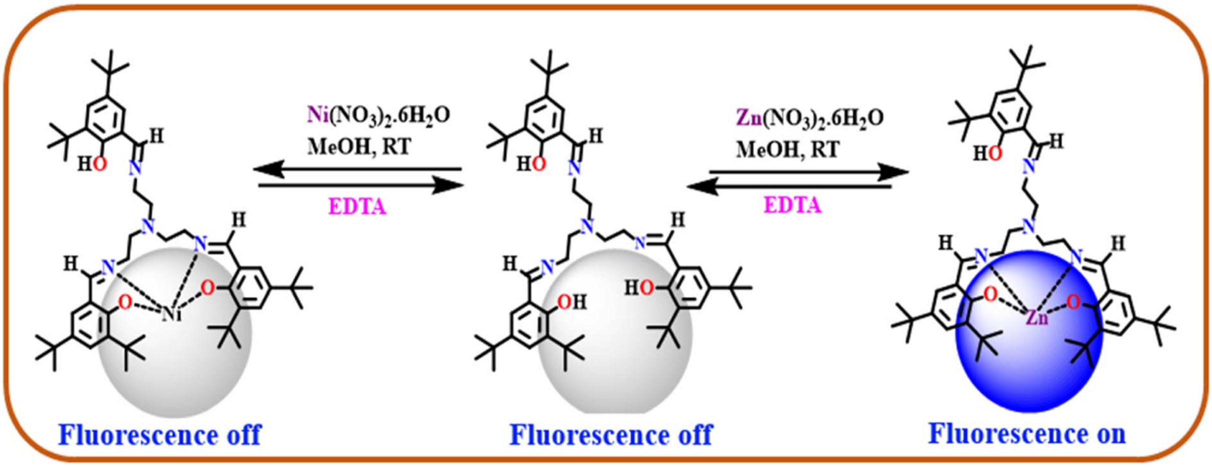

Scheme 2 Proposed sensing mechanism of probe **L**.

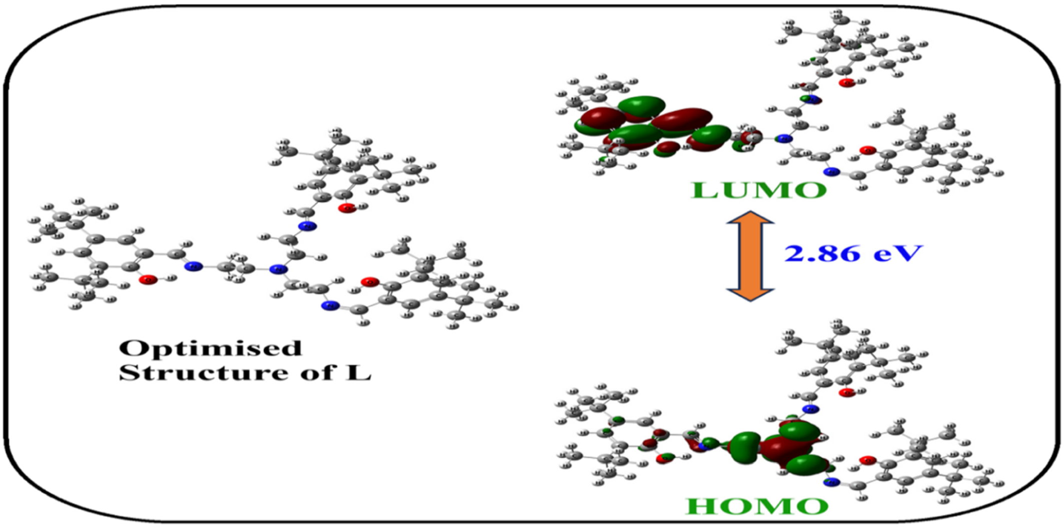

Fig. 10 Optimized geometry, frontier molecular orbitals and HOMO–LUMO energy gap of the ligand **L**.

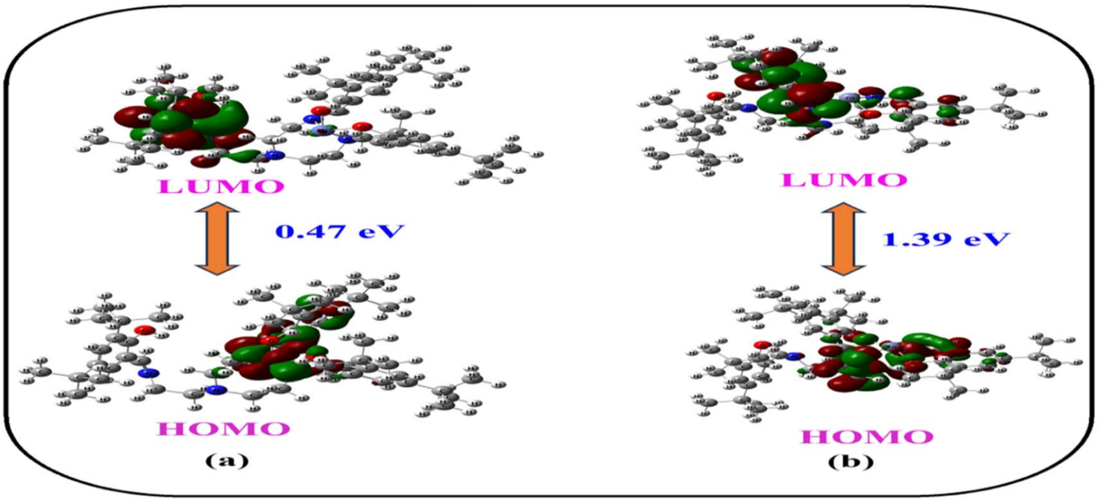

Fig. 11 Frontier molecular orbitals and HOMO–LUMO energy gaps in (a) **L**-Ni^{2+} and (b) **L**-Zn^{2+} complexes.

4 Applications of the chemosensor L

4.1 Application of the chemosensor L in real sample analysis

To examine the Ni^{2+} and Zn^{2+} sensing capabilities of the current chemosensor **L** in actual water samples, we tested the probe **L** in waste-water and got some findings. To evaluate its sensing in a variety of genuine samples, known quantities of standard M^{2+} solutions have been added to prepare artificial M^{2+} (M = Ni and Zn) polluted tap water samples. Polluted tap water samples have been treated with known amounts of standard M^{2+} solutions in order to assess its sensing in various samples. Analyte concentrations are brought within the working range by filtration and dilution after the proper pre-treatment. The prepared samples were analyzed using the same UV-vis spectrometer and Spectrofluorometer, and the recovery quantities were determined using the calibration curve (intensity *vs.* conc.) and the Lambert–Beer law. Table 1 shows that the recovered M^{2+} concentration for each sample accurately and closely matches the amount that was spiked. Thus, the receptor **L** might be useful in real-world settings since it could be able to quantitatively identify the M^{2+} ions in real water samples (Table 1).

Table 1 Analysis of Ni^{2+} and Zn^{2+} in waste-water samples by the developed method (mean ± standard deviation, $n = 3$)

Cation	Spiked amount (μM)	Recovered amount (μM)	% Recovery ± SD ($n = 3$)
Ni^{2+}	5	5.12	102.4 ± 0.98
	10	10.97	109.7 ± 0.89
	20	20.06	100.3 ± 1.5
Zn^{2+}	5	5.10	102 ± 0.96
	10	9.8	98 ± 1.4
	20	19.7	98.5 ± 0.81

4.2 Detection of Zn^{2+} in food samples

This study looked at probe **L**'s capacity to measure Zn^{2+} ions in a range of fruit and vegetable samples. At first, there were no measurable amounts of Zn^{2+} in the food samples that were gathered. Controlled studies were conducted utilizing digested fruit and vegetable extracts to guarantee full release of metal ions for analysis in order to further confirm the use of probe **L** for Zn^{2+} sensing. A robust interaction between the probe and Zn^{2+} ions was demonstrated by the distinct changes in fluorescence intensity at 480 nm observed when these samples were treated with probe **L**.

The samples, which included apple, guava, mango, beetroot, lemon, potato, carrot, and pomegranate, were mixed with standard Zn^{2+} solutions at three different concentrations (10, 50, and 100 μM) in order to perform a quantitative study. The conventional addition approach, which reduces matrix effects that can distort analytical results and are frequently brought on by complicated food compositions, was then employed to assess the fluorescence response. Compared to conventional calibration techniques, this method guarantees more accurate quantification of the target analyte.

According to Table 2, the expected recovery values for Zn^{2+} in all food items under investigation had relative standard deviations (RSD) ranging from 0.28% to 3.63%, with values falling between 78% and 99.9%. These findings demonstrate the accuracy, precision, and dependability of probe **L** in identifying Zn^{2+} ions in actual food matrices. Probe **L** is a helpful fluorescent sensor for tracking Zn^{2+} contamination in food samples because its recoveries are below allowable analytical values. This illustrates the potential applications of the probe for environmental and public health monitoring as well as for evaluating food safety.

Table 2 Determination of Zn^{2+} in food samples by L

Sample name	Spiked (μM) Zn^{2+}	Found (μM) Zn^{2+}	Recovery (%) Zn^{2+}	RSD (%) ($n = 2$)
Dragon fruit	10	9.4	94	1.50
	50	48.9	97.8	0.58
	100	98.6	98.6	0.43
Beetroot	10	9	90	3.14
	50	48.7	97.4	0.58
	100	98.5	98.5	0.29
Carrot	10	9.7	97	1.45
	50	49.0	98	0.58
	100	97.8	97.8	0.43
Orange	10	7.8	78	3.63
	50	48.5	97	0.58
	100	98.7	98.7	0.29
Pomegranate	10	9.7	97	1.45
	50	49.9	99.8	0.57
	100	98.5	98.5	0.29
Mango	10	8.5	85	1.66
	50	47.6	95.2	0.59
	100	99.8	99.8	0.28
Apple	10	9.2	92	1.53
	50	49.4	98.8	0.57
	100	97.6	97.6	0.29
Lichi	10	9.9	99	1.42
	50	49.5	99	0.57
	100	99.9	99.9	0.28

4.3 Fingerprint application

Fingerprints are unique ridge patterns present on the fingertips that remain unchanged throughout life, making them a powerful tool for personal identification and forensic investigations. Their detection and development are necessary as latent fingerprints, often left on surfaces due to sweat, sebum, and oils, are invisible to the naked eye but can provide crucial evidence in linking individuals to crime scenes. Among various visualization techniques, the powder development method is widely used because it is simple, inexpensive, and highly effective on non-porous surfaces. The powder adheres to fingerprint residues, creating clear ridge patterns that can be easily lifted and preserved. In this study, we have utilised the Schiff base (**L**) for use in Latent Fingerprint (LFP) development.

After being prepared as a fine powder, compound **L** was employed right away to dust latent fingerprints to aid in their development. Following development, the LFPs were seen at 396 nm under UV illumination. Images of LFPs were created on a variety of surfaces, including as sunmica, glass, plastic, coins, and laptop surfaces. The photographs displayed clear papillary ridges, and the chemical was able to identify fingerprint profiles. Fig. 12 shows the photos taken with the OnePlus Nord 4 smartphone.

Three levels can be distinguished in fingerprint patterns. The primary identification of cores and deltas is part of Level I. Features such as ridges, bifurcations, hooks, bridges, *etc.* are identified at Level II. Level III has sufficient information to uniquely identify a person, such as ridge path deviations and sweat pores. To identify a person, the LFPs developed with compound **L** were examined for these values. Fig. 12 indicates that the LFPs developed using the compound **L** were high-resolution and showed less background interference. The compound shows up to three levels of fingerprint pattern identification over various surfaces. The images were taken under visible illumination and immediately under UV 396 nm illumination. The images were clear and readable (Fig. 13). The compound's ability to capture intricate details at various levels

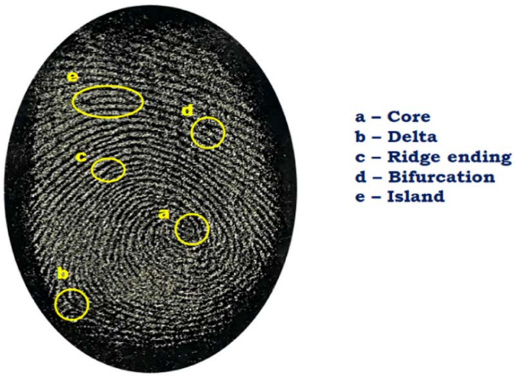

Fig. 12 Latent fingerprint developed using L and analyzed for identification.

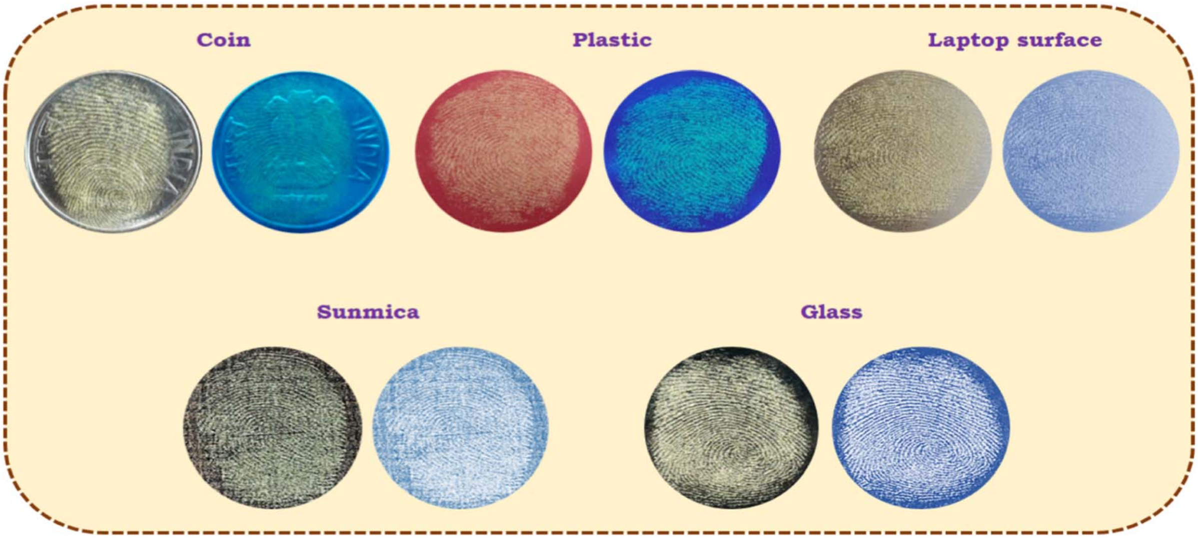

Fig. 13 Latent fingerprint developed using **L** on various surfaces under visible (left) and UV illumination (right) at 396 nm.

is particularly advantageous for forensic and law enforcement efforts, enhancing the precision and dependability of individual identification based on latent fingerprints.

The applicability of the developed probe, **L** in latent fingerprint visualization was systematically evaluated to assess its potential as a colorimetric-based imaging material. The probe exhibited excellent performance in revealing clear and well-defined ridge patterns on various substrates, including glass, paper, and metallic surfaces. This enhanced visualization can be attributed to the probe **L**'s strong affinity toward fingerprint residues, which typically consist of a complex mixture of amino acids, lipids, fatty acids, and moisture. The presence of functional groups such as imine (C═N) and phenolic –OH in the probe facilitates intermolecular interactions, including hydrogen bonding and weak coordination, with these constituents, enabling efficient adherence to the ridge regions.

5 Molecular docking

The molecular docking study has been performed to provide molecular-level insight into the interaction capability of the probe, particularly through its imine (C═N), phenolic –OH, and aromatic functionalities. Such interactions are relevant not only for biomolecular systems but also for understanding the probe **L**'s behaviour in complex environments, including real samples and fingerprint matrices. Recent studies have demonstrated that Schiff base-derived probes can exhibit meaningful non-covalent interactions with biomolecules, supporting their broader applicability beyond sensing.[58]

With a docking score of -10.36 kcal mol^{-1}, molecular docking tests conducted with ArgusLab 4.0.1 against the FP domain of the human PI31 proteasome inhibitor (PDB ID: 4OUH) showed a significant binding affinity of the probe **L**. A crucial hydrogen connection between the nitrogen atom of Lys1 and the oxygen atom of an unnamed residue (1088) at a distance of 1.79 Å was found using two-dimensional interaction analysis in Discovery Studio. Furthermore, the ligand–protein complex was further strengthened by stabilizing hydrophobic and van der Waals interactions with residues Asp62, Ile63, Leu65, Leu66, Asp217, Val222, and Asn218. The ligand **L**'s deep insertion into the binding pocket was verified by three-dimensional imaging. It matched well with the hydrophobic core of the FP domain and formed complementary interactions inside the active site groove. According to the structural insights, the ligand **L** uses a combination of polar and non-polar contacts to produce stable anchoring, which may have a substantial inhibitory effect on the proteasomal regulation linked to PI31. These results demonstrate the potential of the **L** as a framework for therapeutic development in proteasome dysregulated disorders (Fig. 14).

Using ArgusLab 4.1.0, molecular docking simulations were performed to assess **L**'s binding affinity for cyclooxygenase, another protein (active site of COX-2; PDB ID: 1PXX). A computed binding energy of -12.77 kcal mol^{-1} indicated a strong binding affinity, according to the docking data. A complex network of stabilizing interactions, including a crucial hydrogen bond between the nitrogen atom of Lys114 and the oxygen atom of residue 35 454 of amino acids, with a bond distance of 2.51 Å, was revealed by two-dimensional interaction profiling in Discovery Studio (Fig. 15, right). The deep accommodation of **L** within the COX-2 active site pocket was validated by the three-dimensional model (Fig. 15, left), indicating a robust and targeted interaction. Its putative function as a selective COX-2 inhibitor is supported by structural insights that show the ligand **L** achieves stable anchoring through both polar and hydrophobic interactions. These results suggest that **L** constitutes a viable framework for the development of anti-inflammatory and analgesic therapies, given the crucial role of COX-2 in inflammation and pain signalling. These results suggest that **L** may serve as a promising structural scaffold for the further development of anti-inflammatory and analgesic agents targeting COX-2-mediated pathways. However,

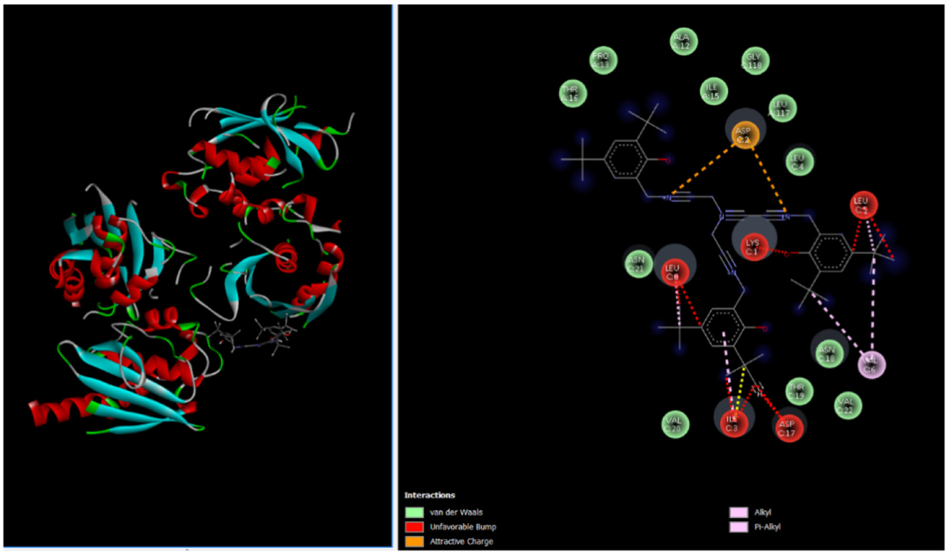

Fig. 14 Molecular docking of the novel ligand with the FP domain of human *PI31 proteasome inhibitor* (PDB ID: 4OUH).

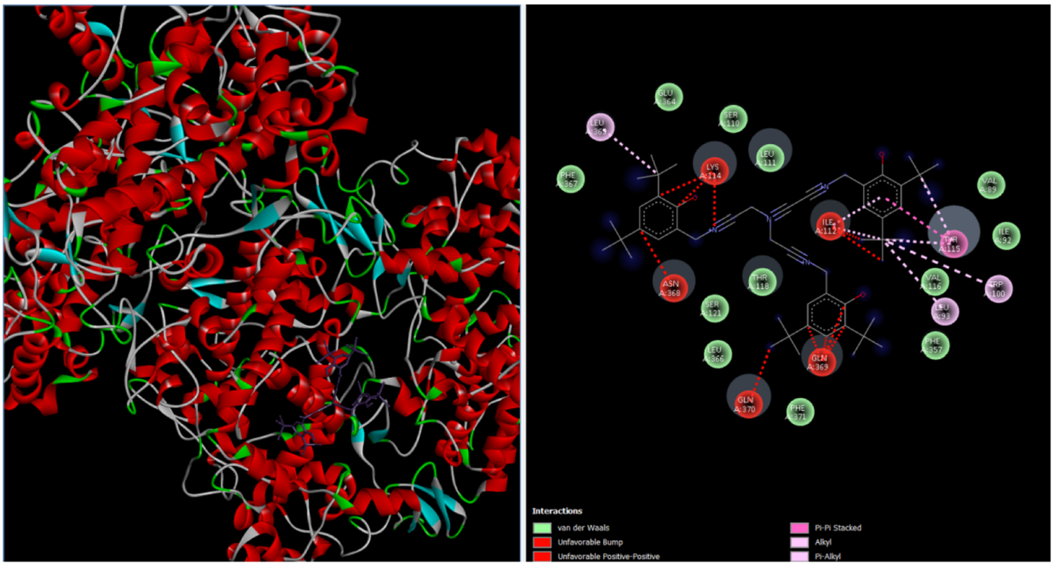

Fig. 15 Molecular docking of the novel ligand with the *cyclooxygenase active site of COX-2* (PDB ID: 1PXX).

additional experimental validation is required to establish its biological efficacy and pharmacological relevance (Fig. 15).

The human 3SFH protein (PDB ID: 3SFH), a verified therapeutic target linked to cancer and other clinical diseases, was the target of molecular docking investigations using the same chemical **L**. The Protein Data Bank provided the crystal structure, which depicts an inhibitor complex generated from HDAC8 amino acids. ArgusLab 4.1.0 was used for docking simulations, while Discovery Studio was used to display and analyze the protein-compound complexes that were produced. With a docking score of -10.50 kcal mol^{-1}, the molecule demonstrated a highly favorable binding shape, suggesting considerable affinity for the 3SFH active site. A crucial hydrogen bond with Ser63 at a bond distance of 2.89 Å was discovered after thorough interaction profiling. The complex's overall stability was further enhanced by the observation of several stabilizing contacts, including as van der Waals, hydrophobic, and electrostatic interactions with important residues like Glu66, Val91, and Arg163. The promise of this novel chemical as a promising inhibitor of 3SFH is highlighted by the combination of a great docking score and particular residue–level interactions. These computational findings suggest the potential of the studied scaffold for further exploration against disorders associated with 3SFH and provide preliminary structural insight for subsequent experimental validation through appropriate *in vitro* and *in vivo* investigations (Fig. 16).

Likewise, ligand **L**'s molecular docking experiments with another protein (PDB ID; 3RCD), a HER2 receptor linked to

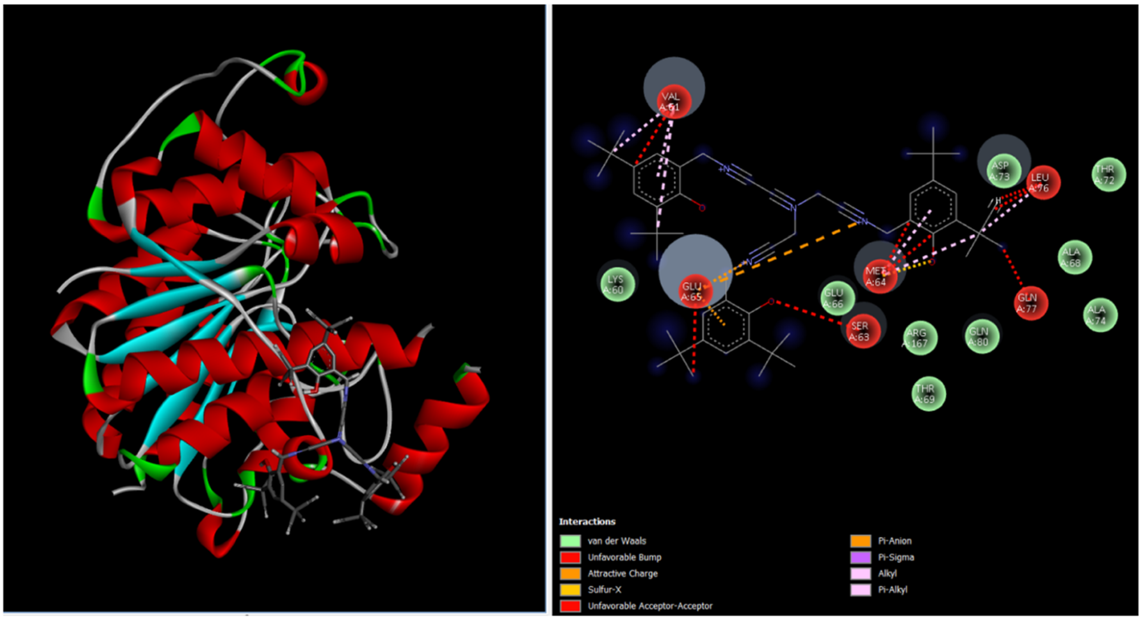

Fig. 16 Molecular docking of ligand **L** with the active site of *HDAC8* (PDB ID: 3SFH).

breast cancer. The MMFF94 force field in ArgusLab 4.0.1 was used to minimize the compound's energy, and ArgusLab was used to perform docking simulations using a grid box enclosing the active site. Discovery Studio was used to display and evaluate the resultant protein-compound complexes. The molecule demonstrated a strong and stable affinity with a docking score of -13.58 kcal mol^{-1}, indicating a very favorable binding conformation within the 3RCD active site. In addition to several stabilizing contacts, such as attractive charge interactions with PHE E:1046, hydrophobic interactions with LEU E:1047, ILE E:1107, and VAL E:1111, and a Pi-Cation interaction with a positively charged residue, a thorough interaction analysis showed the formation of a critical hydrogen bond at a distance of 2.46 Å. The observed docking score along with favorable residue–level interactions suggests that the compound may exhibit potential binding affinity within the HER2 active site. These *in silico* findings provide preliminary structural insights into ligand–target recognition and may support further optimization and biological evaluation of this scaffold against HER2-positive breast cancer. However, experimental validation through appropriate *in vitro* and *in vivo* studies is necessary to substantiate its pharmacological relevance (Fig. 17).

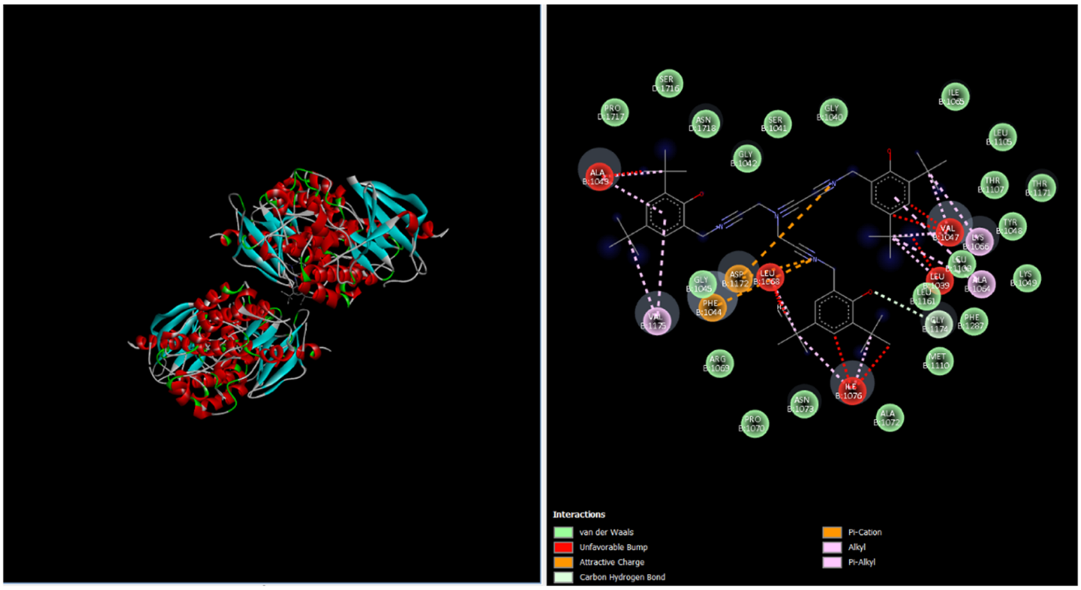

Fig. 17 Molecular docking of the ligand **L** with the active site of *HER2* (PDB ID: 3RCD).

Table 3 Comparison of some previously reported colorimetric chemosensors for Ni^{2+} ions

No.	Sensor type	Selectivity	Detection limit (LOD)	Binding constant	Solvent medium	Sensing mechanism	pH range	Structure	Ref.
1	Coumarin Schiff base	Ni^{2+} colorimetric sensor	14.7×10^{-7}	2.9×10^{4} M^{-1}	MeCN–H_2O	Fluorescence quenching	—	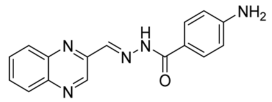	63
3	Naphthyridine Schiff base	Ni^{2+} turn-off sensing	5.6×10^{-7}	2.43×10^{-7} M	Aqueous-EtOH (1 : 1), pH 7.0	ET, CT, PET, ESIPT	2.0–12.0	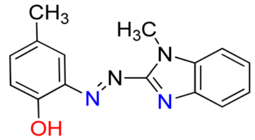	64
4	Hydroxybenzylidene sensor (BHEP)	Ni^{2+} colorimetric	17.79×10^{-7}	3.69×10^{5} M^{-1}	Methanol–Tris–HCl buffer (1 : 1, pH 7.2)	CHEF and FRET	2 to 11	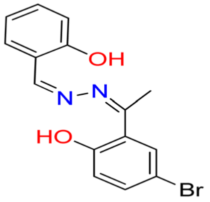	65
5	Coumarin based sensor	Ni^{2+} colorimetric sensor	0.5 μM	2.343×10^{4} M^{-1}	HCl–EtOH (2 : 1), pH 5–6	ICT	—	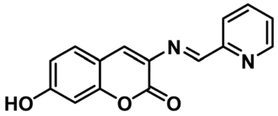	66
6	Acetylpyridine based sensor	Ni^{2+} colorimetric sensor	3.61×10^{-7}	1.13×10^{8} M^{-1}	CH_3OH–H_2O; 1 : 1, v/v	ICT, LMCT	1–12	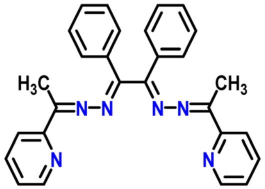	67
7	4-Formylbenzoic acid based sensor	Ni^{2+} colorimetric sensor	3×10^{-7}	1.54×10^{8} $M^{-1/2}$	CH_3OH–H_2O; 1 : 1, v/v	LMCT, CHEF	2 to 12	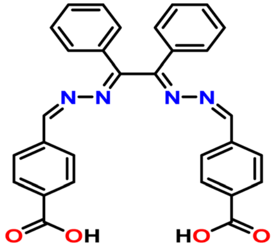	56

Table 3 (*Contd.*)

No.	Sensor type	Selectivity	Detection limit (LOD)	Binding constant	Solvent medium	Sensing mechanism	pH range	Structure	Ref.
8	Julolidine–hydrazinylpyridine Schiff base	Ni^{2+}, Cu^{2+}, Zn^{2+}, Co^{2+}	Not specified	$1.35 \times 10^5\ M^{-1}$	50% EtOH–Tris–HCl buffer (pH 7.4)	Esipt, IMHB	7.40	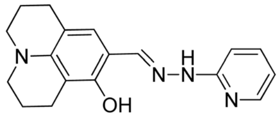	68
9	Pyridine-dicarboxylate hydrazone Schiff base (DAS)	Highly selective for Ni^{2+}	0.14 μM	$3.07 \times 10^3\ M^{-2}$	MeOH–PBS buffer (5 : 1, pH 7.4)	CT	3–11	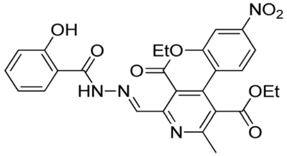	69
10	3,5-Di-*tert*-butyl-2-hydroxybenzaldehyde	Ni^{2+} Colorimetric	9.4×10^{-7} M	$1.86 \times 10^3\ M^{-1/2}$	Methanol–Tris–HCl buffer (1 : 1, pH 7.2)	LMCT	6–8	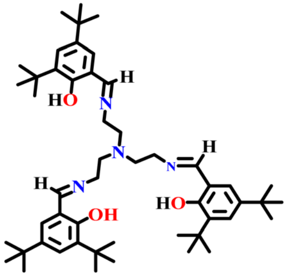	Present study

Table 4 Comparison of some previously reported fluorometric chemosensors for Zn^{2+} ions

No.	Sensor type	Selectivity	Detection limit (LOD)	Binding constant	Solvent medium	Sensing mechanism	pH range	Structure	Ref.
1	Hydroxy-benzaldehyde	Zn^{2+} fluorometric CHEF (off–on–off)	5.0×10^{-9}	3.21×10^{-6} M^2	H2O : CH_3CN (1 : 1)	ESIPT	2–10	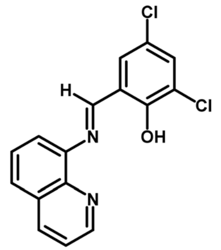	70
2	4-Quinoline carboxaldehyde	Zn^{2+} fluorometric PET, CHEF (turn-on)	2.04×10^{-6}	5×10^9 M^{-2}	CH_3OH-tris buffer (1/1, v/v)	PET, CHEF	1 to 12	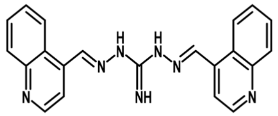	71
3	3-Methoxysalicylaldehyde	Zn^{2+} fluorometric CHEF (turn-on)	11.9×10^{-6}	4.5×10^3 M^{-1}	DMSO 1 : 1	CHEF, ICT	2–12	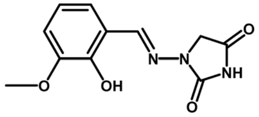	72
4	4-(*N*,*N*-Diethyl)-2-hydroxybenzaldehyde	Zn^{2+} fluorometric C=N, CHEF (turn-on)	8.6×10^{-9}		DMF 1 : 1	CHEF	—	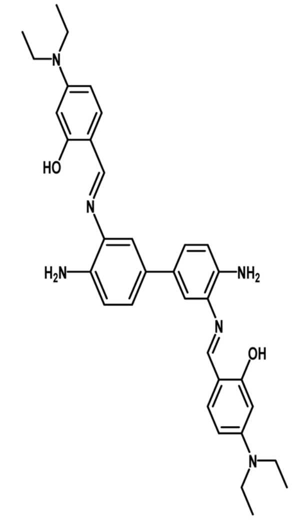	73

Table 4 (*Contd.*)

No.	Sensor type	Selectivity	Detection limit (LOD)	Binding constant	Solvent medium	Sensing mechanism	pH range	Structure	Ref.
5	5-Bromosalicylaldehyde	Zn^{2+} fluorometric C═N, CHEF (turn-on)	1.59 μM	$4.24 \times 10^4\ M^{-1}$		CHEF, PET	2–12	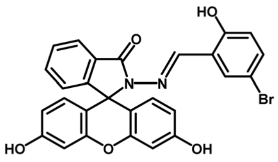	74
6	4-Methyl-2,6-bis(1-(2-piperidinoethyl) iminomethyl)-phenol	Zn^{2+} fluorometric	—	$\sim 10^4\ M^1$	Acetonitrile (1 : 2)	PET	—	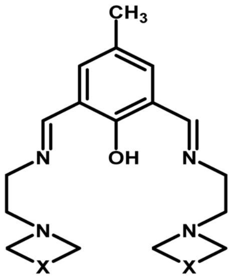	75
7	3,5-Di-*tert*-butyl-2-hydroxybenzaldehyde	Zn^{2+} fluorometric	4.68×10^{-7} M	$1.2 \times 10^5\ M^{-1/2}$	Methanol–Tris–HCl buffer (1 : 1, pH 7.2)	CHEF	—	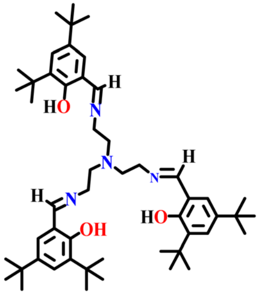	Present study

The obtained binding energies fall within the typical range (-5 to -10 kcal mol^{-1}), stable ligand–protein interactions. The docking poses exhibit chemically meaningful interactions, including hydrogen bonding and hydrophobic contacts, consistent with established ligand–protein binding patterns. The involvement of key functional groups (C=N, –OH) aligns with both spectroscopic binding evidence and previously reported docking studies of structurally related compounds.[59]

The calculated binding affinities of the probe for the selected targets were -10.36, -12.77, -10.50, and -13.58 kcal mol^{-1}. These values were compared with recent reports in the literature, where binding energies in the range of -5 to -10 kcal mol^{-1} are generally associated with moderate to strong ligand–protein interactions, while values beyond -10 kcal mol^{-1} indicate highly stable and favorable binding. The obtained values, particularly those approaching -12 to -13 kcal mol^{-1}, clearly fall within or exceed the range reported for potent ligand–protein interactions, thereby confirming the strong binding capability and reliability of the docking results.

The docking poses exhibit chemically meaningful interaction profiles, including hydrogen bonding and hydrophobic contacts involving key functional groups such as the imine (C=N), phenolic –OH, and aromatic rings. These interaction modes are consistent with established ligand–protein binding patterns reported in recent studies. The probe also adopts a stable conformation within the binding pocket without steric hindrance, further supporting the structural validity of the docking predictions.[60–62]

6 Comparison of the performance of L with other reported fluorescent and colorimetric chemosensors

Finding a single probe that can be used for both colorimetric Ni^{2+} detection and "turn-on" fluorometric Zn^{2+} ion detection is rare in the literature. Among the attractive analytical features that distinguish our system from the others are its high sensitivity, broad linear range, excellent selectivity, low detection limit, user-friendly technology, good solubility, sensitive visualization, and exceptional practical applicability. Furthermore, using less dangerous chemicals and without creating any hazardous by-products, our proposed chemosensor **L** can be synthesized in a single step. We have included two tables (Tables 3 and 4) that compare colorimetric detection of Ni^{2+} ions and turn-on fluorometric detection of Zn^{2+} ions with different verified optical sensors.

7 Conclusion

In conclusion, we have successfully demonstrated here a tripodal N_4O_3 donor tris-Schiff base hemi-salen molecular probe **L**, made from 3,5-di-*tert*-butyl-2-hydroxybenzaldehyde and tris-(2-aminoethyl) amine for sensitive and specific colorimetric detection of Ni^{2+} and turn-on fluorometric detection of Zn^{2+} in an aqueous solution over a number of competing cations, with detection limits of 9.4×10^{-7} M and 4.68×10^{-7} M, respectively. Job-plot, FT-IR, and ESI-mass spectral analysis and DFT studies all supported a 1 : 1 stoichiometry between Zn^{2+} and **L**, & Ni^{2+} and **L** The reversible reactivity of **L** towards the Ni^{2+} and Zn^{2+} ions was tested by Na_2EDTA. Furthermore, **L** is capable of operating across a wide pH range and is useful for identifying and measuring Ni^{2+} and Zn^{2+} in food and environmental materials. It helps to create latent fingerprints that can be used in forensic applications. An initial computational understanding of potential biomolecular interactions of **L** have been studies through molecular docking.

Author contributions

Dishen Kumar: conceptualization, methodology, investigation. Srishti Dutta: investigation. Rajat Kumar Roy: investigation. Abhilash Pandey: formal analysis. Devanand Sahu: conceptualization. Vanshika Sharma: validation. Anjali Suryavanshi: biological studies. Goutam Kumar Patra: writing the manuscript, conceptualization, supervision.

Conflicts of interest

Authors declare no conflicts of interest.

Data availability

The datasets generated during and/or analysed during the current study are available from the corresponding author on reasonable request.

Supplementary information (SI) is available. See DOI: https://doi.org/10.1039/d6ra01601d.

Acknowledgements

G. K. P would like to thank the Department of Science and Technology (SR/FST/CSI-264/2014 and EMR/2017/0001789) and Department of Biotechnology, Government of India, New Delhi for financial support.

References

1 M. Li, Q. Shi, N. Song, Y. Xiao, L. Wang, Z. Chen and T. D. James, *Chem. Soc. Rev.*, 2023, **52**, 5827–5860.
2 M. K. Goshisht, G. K. Patra and N. Tripathi, *Mater. Adv.*, 2022, **3**, 2612–2669.
3 J. Briffa, E. Sinagra and R. Blundell, *Heliyon*, 2020, **6**, e04691.
4 F. Nielsen, *Adv. Nutr.*, 2021, **12**, 281–282.
5 G. Genchi, A. Carocci, G. Lauria, M. S. Sinicropi and A. Catalano, *Int. J. Environ. Res. Public Health*, 2020, **17**, 679.
6 A. Patra, R. P. Singh, B. K. Singh and A. Kumar, *Int. J. Environ. Sci. Nat. Resour.*, 2024, **6**, 465–467.
7 M. Sahu, A. K. Manna, S. Chowdhury and G. K. Patra, *RSC Adv.*, 2020, **10**, 44860–44875.
8 A. Chowdhury, P. Howlader and P. S. Mukherjee, *Chem. Eur. J.*, 2016, **22**, 1424–1434.
9 B. Zambelli, F. Musiani, S. Benini and S. Ciurli, *Acc. Chem. Res.*, 2011, **44**, 520–530.

10 S. W. Ragsdale, *J. Biol. Chem.*, 2009, **284**, 18571–18575.
11 R. J. Maier, *Biochem. Soc. Trans.*, 2005, **33**, 83–85.
12 K. S. Kasprzak, F. W. Sunderman and K. Salnikow, *Mutat. Res.*, 2003, **533**, 67–97.
13 P. H. Kuck, *Mineral Commodity Summaries: Nickel*, United States Geological Survey, 2006.
14 W. Lee, K. A. Davis, R. L. Rettmer and R. F. Labbe, *Am. J. Clin. Nutr.*, 1988, **48**, 286.
15 X. Q. Liu, X. Zhou, X. Shu and J. Zhu, *Macromolecules*, 2009, **42**, 7634.
16 F. Robert-Peillard, E. M. El Mouchtari, D. Bonne, S. Humbel, J.-L. Boudenne and B. Coulomb, *Spectrochim. Acta A Mol. Biomol. Spectrosc.*, 2022, **275**, 121170.
17 G. Genchi, A. Carocci, G. Lauria, M. S. Sinicropi and A. Catalano, *Int. J. Environ. Res. Public Health*, 2020, **17**, 679.
18 H. Huang, F. P. Shi, Y. Li, L. Niu, Y. Gao and S. M. Shah, *Sens. Actuators, B*, 2013, **178**, 532–538.
19 A. Pandey, D. Sahu, R. K. Roy, S. Dutta, D. Kumar, V. Sharma, U. K. Das, A. Verma and G. K. Patra, *Polyhedron*, 2025, **283**, 117864.
20 A. Kumar, V. Saini, M. Mohan and M. Kamboj, *Microchem. J.*, 2022, **181**, 107798.
21 X. Zhong, Z. Li, R. Shi, L. Yan, Y. Zhu and H. Li, *ACS Appl. Nano Mater.*, 2022, **5**, 13998–14020.
22 V. Sharma, M. Sahu, A. K. Manna, D. De and G. K. Patra, *RSC Adv.*, 2022, **12**, 34226–34235.
23 K. H. Falchuk, *Mol. Cell. Biochem.*, 1998, **188**, 41–48.
24 W. Maret, C. Jacob, B. L. Vallee and E. H. Fischer, *Proc. Natl. Acad. Sci. U.S.A.*, 1999, **96**, 1936–1940.
25 H. H. Sandstead, *J. Trace Elem. Exp. Med.*, 2003, **16**, 165–173.
26 J. A. Duce, A. Tsatsanis, M. A. Cater, *et al.*, *Cell*, 2010, **142**, 857–867.
27 E. M. Álvarez, R. S. Otero, A. H. Ameijeiras, A. M. L. Real and J. L. L. García, *Biochim. Biophys. Acta*, 2002, **1586**, 155–168.
28 T. Liu and S. Liu, *Anal. Chem.*, 2011, **83**, 2775–2785.
29 S. Goswami, A. K. Das, K. Aich, A. Manna, S. Maity, K. Khanra and N. Bhattacharyya, *Analyst*, 2013, **138**, 4593–4598.
30 J. Wan, W. Duan, K. Chen, Y. Tao, J. Dang, K. Zeng, Y. Ge, J. Wu and D. Liu, *Sens. Actuators, B*, 2018, **255**, 49–56.
31 J. Y. Koh, S. W. Suh, B. J. Gwag, Y. Y. He, C. Y. Hsu and D. W. Choi, *Science*, 1996, **272**, 1013–1016.
32 H.-X. Wang, C.-W. Wei, X.-J. Wang, H.-F. Xiang, X.-Z. Yang, G.-L. Wu and Y.-W. Lin, *Spectrochim. Acta A Mol. Biomol. Spectrosc.*, 2021, **250**, 119378.
33 S. L. C. Ferreira, A. S. Queiroz, M. S. Fernandes and H. C. dos Santos, *Spectrochim. Acta, Part B*, 2002, **57**, 1939–1950.
34 A. Ali, H. Shen and X. Yin, *Anal. Chim. Acta*, 1998, **369**, 215–223.
35 R. N. Goyal, V. K. Gupta and S. Chatterjee, *Sens. Actuators, B*, 2010, **149**, 252–258.
36 M. H. Mashhadizadeh, M. Pesteh, M. Talakesh, I. Sheikhshoaie, M. M. Ardakani and M. A. Karimi, *Spectrochim. Acta, Part B*, 2008, **63**, 885–888.
37 W. Dos Santos, D. T. Gimenes, E. M. Richter and L. Angnes, *Quim. Nova*, 2011, **34**, 1753–1761.
38 H. Ghafoor, A. Hussain, S. Hussain, Z. Shafiq, K. Mahmood, N. Ahmed, M. Yar, K. Ayub, X. Hao, Z. Changjin and A. Ali, *J. Mol. Struct.*, 2024, **1308**, 138082.
39 C. W. Kayogolo, M. R. Vegi, B. B. L. Srivastava and M. G. Sahini, *J. Coord. Chem.*, 2022, **75**, 1–48.
40 F. Xu, B. Hu, X.-X. Wang, J. Geng and W. Huang, *J. Coord. Chem.*, 2012, **65**, 2201–2210.
41 V. Sharma, S. Dutta, D. Sahu, A. Pandey, D. Kumar, J. M. Bag and G. K. Patra, *Curr. Nanosci.*, 2025, **21**, 358–372.
42 R. Chandra, A. K. Manna, K. Rout, J. Mondal and G. K. Patra, *RSC Adv.*, 2018, **8**, 35946–35958.
43 S. Thapa, K. R. Singh and S. S. Pandey, *Chemosensors*, 2025, **13**, 288.
44 R. Chandra, A. K. Manna, M. Sahu, K. Rout and G. K. Patra, *Inorg. Chim. Acta*, 2020, **499**, 119192.
45 A. K. Manna, S. Chowdhury and G. K. Patra, *Dalton Trans.*, 2019, **48**, 12336–12348.
46 V. Sharma, B. Sahu, U. K. Das and G. K. Patra, *Inorg. Chim. Acta*, 2023, **552**, 121491.
47 A. Ghorai, S. S. Thakur and G. K. Patra, *RSC Adv.*, 2016, **6**, 108717–108725.
48 D. Li, *J. Photochem. Photobiol., A*, 2025, **474**, 116958.
49 B. N. Revanna, M. Madegowda and S. Anand, *J. Mol. Structure*, 2025, **1337**, 142183.
50 V. Yadav, R. Kumar and V. K. Bhardwaj, *Polyhedron*, 2025, 117829.
51 P. Sahu, A. K. Chaturwedi, A. R. Patel, A. Pandey, V. Sharma, B. W. Matore, J. Singh, P. P. Roy, M. Hait and G. K. Patra, *RSC Adv.*, 2025, **15**, 30466–30481.
52 V. Sharma, S. Savita and G. K. Patra, *RSC Adv.*, 2024, **14**, 3289–3303.
53 R. Chandra, A. Dutta, A. K. Manna, K. Rout, J. Mondal and G. K. Patra, *Inorg. Chim. Acta*, 2019, **496**, 119042.
54 R. Chandra, M. Sahu, A. K. Manna, K. Rout, S. Chowdhury and G. K. Patra, *J. Photochem. Photobiol., A*, 2020, **389**, 112179.
55 S. Dutta, D. Kumar, A. Pandey, S. Manna, S. Maiti Choudhury, D. Sahu, V. Sharma, N. Kumari and G. K. Patra, *New J. Chem.*, 2025, **49**, 11906–11919.
56 D. Kumar, S. Dutta, A. Pandey, V. Sharma, D. Sahu, S. Manna, S. Maiti Choudhury and G. K. Patra, *Chem.–Asian J.*, 2025, **20**, e00779.
57 V. Sharma, M. Sahu, A. K. Manna, D. De and G. K. Patra, *RSC Adv.*, 2022, **12**, 34226–34235.
58 L. Ivanova and M. Karelson, *Molecules*, 2022, **27**(24), 9041.
59 G. S. Li, K. S. Yang, R. L. Blankenship, D. Chia-Chuan Cho, Xu Shiqing, H. Wang and L. R. Wenshe, *Front. Chem.*, 2022, **10**, 816576.
60 N. A. Khaled, S. A. Ahmed, M. A. Ibrahim, O. M. Ahmed, N. A. Mohamed and N. M. Khalifa, *Sci. Rep.*, 2026, **16**, 10985.
61 Z. Sadeghian, M. Bayat and D. Gheidari, *Nanoscale Adv.*, 2025, **7**(18), 5760–5783.
62 S. Sing, H. K. Srivastava, G. Kishor, H. Singh, P. Agrawal and G. P. Raghava, *BioRxiv*, 2017, 212514.
63 L. Wang, D. Ye and D. Cao, *Spectrochim. Acta A Mol. Biomol. Spectrosc.*, 2012, **90**, 40–44.

64 M. Ashraf, M. Islam, M. Khalid, A. P. Davis, M. T. Ahsan, M. Yaqub, A. Syed, A. M. Elgorban, A. H. Bahkali and Z. Shafiq, *Sci. Rep.*, 2021, **11**, 19242.

65 A. Kumar, B. Mohan, K. Modi, M. A. U. Din and S. Kumar, *J. Mol. Struct.*, 2022, **1268**, 133609.

66 J. Jiang, C. Gou, J. Luo, C. Yi and X. Liu, *Inorg. Chem. Commun.*, 2012, **15**, 12–15.

67 D. Kumar, S. Dutta, A. Pandey, D. Sahu, V. Sharma, U. K. Das and G. K. Patra, *J. Mol. Struct.*, 2025, 143933.

68 H. Liu, S. Ding, Q. Lu, Y. Jian, G. Wei and Z. Yuan, *ACS Omega*, 2022, **7**, 7585–7594.

69 R. Bawa, S. Negi, B. Singh, B. Pani and R. Kumar, *RSC Adv.*, 2023, **13**, 15391–15400.

70 D. Sarkar, A. Pramanik, S. Jana and P. Karmakar, *Sens. Actuators, B*, 2015, **209**, 138–146.

71 K. Rout, A. K. Manna, M. Sahu and G. K. Patra, *Inorg. Chim. Acta*, 2019, **486**, 733–741.

72 M. S. Kim, T. G. Jo, M. Yang, J. Han, M. H. Lim and C. Kim, *Spectrochim. Acta A Mol. Biomol. Spectrosc.*, 2019, **211**, 34–43.

73 M. Kumar, A. Kumar, M. K. Singh, S. K. Sahu and R. P. John, *Sens. Actuators, B*, 2017, **241**, 1218–1223.

74 B. Das, A. Jana, A. D. Mahapatra, D. Chattopadhyay, A. Dhara, S. Mabhai and S. Dey, *Spectrochim. Acta A Mol. Biomol. Spectrosc.*, 2019, **212**, 222–231.

75 P. Roy, K. Dhara, M. Manassero and P. Banerjee, *Inorg. Chim. Acta*, 2009, **362**, 2927–2932.